universe

MDPI

Article

A PeVatron Candidate: Modeling the Boomerang Nebula in X-ray Band

Xuan-Han Liang [1,2], Chao-Ming Li [1,2], Qi-Zuo Wu [1,2], Jia-Shu Pan [1,2] and Ruo-Yu Liu [1,2,*]

[1] Department of Astronomy, Nanjing University, 163 Xianlin Avenue, Nanjing 210023, China
[2] Key Laboratory of Modern Astronomy and Astrophysics, Nanjing University, Ministry of Education, Nanjing 210093, China
* Correspondence: ryliu@nju.edu.cn

Abstract: Pulsar wind nebula (PWN) Boomerang and the associated supernova remnant (SNR) G106.3+2.7 are among candidates for the ultra-high-energy (UHE) gamma-ray counterparts published by LHAASO. Although the centroid of the extended source, LHAASO J2226+6057, deviates from the pulsar's position by about 0.3°, the source partially covers the PWN. Therefore, we cannot totally exclude the possibility that part of the UHE emission comes from the PWN. Previous studies mainly focus on whether the SNR is a PeVatron, while neglecting the energetic PWN. Here, we explore the possibility of the Boomerang Nebula being a PeVatron candidate by studying its X-ray radiation. By modeling the diffusion of relativistic electrons injected in the PWN, we fit the radial profiles of X-ray surface brightness and photon index. The solution with a magnetic field $B = 140\,\mu$G can well reproduce the observed profiles and implies a severe suppression of IC scattering of electrons. Hence, if future observations reveal part of the UHE emission originating from the PWN, we propose to introduce a proton component to account for the UHE emission in light of the recent LHAASO measurement on Crab Nebula. In this sense, Boomerang Nebula would be a hadronic PeVatron.

Keywords: pulsar wind nebulae; X-ray astronomy; gamma-rays; nonthermal radiation

check for updates

Citation: Liang, X.-H.; Li, C.-M.; Wu, Q.-Z.; Pan, J.-S.; Liu, R.-Y. A PeVatron Candidate: Modeling the Boomerang Nebula in X-ray Band. *Universe* **2022**, *8*, 547. https://doi.org/10.3390/universe8100547

Academic Editor: Denis Leahy

Received: 6 September 2022
Accepted: 16 October 2022
Published: 21 October 2022

Publisher's Note: MDPI stays neutral with regard to jurisdictional claims in published maps and institutional affiliations.

Copyright: © 2022 by the authors. Licensee MDPI, Basel, Switzerland. This article is an open access article distributed under the terms and conditions of the Creative Commons Attribution (CC BY) license (https://creativecommons.org/licenses/by/4.0/).

1. Introduction

Cosmic rays (CRs) are mostly protons and nuclei moving nearly at the speed of light. Their origins are not totally clear because as charged particles, their trajectories are deflected by magnetic fields when travelling from sources to the observer. The "knee" structure of the CR spectrum shows up at about 3 PeV, and it is generally believed that CRs with energy below the structure are dominated by the Milky Way. Hence, CR protons can be accelerated up to PeV in Galactic sources, and such CR factories are called PeVatrons. Recently, LHAASO has published a list of ultra-high-energy (UHE, $E_\gamma > 100$ TeV) gamma-ray sources, which are considered as Galactic PeVatron candidates, and for the very first time, we can study such powerful astrophysical objects in the PeV regime [1].

LHAASO J2226+6057 is one of the UHE gamma-ray sources. SNR G106.3+2.7, which was firstly discovered by a radio survey of the Galactic plane [2], is a possible counterpart. Later, this elongated Galactic source was interpreted as a supernova remnant (SNR) with two distinct components, the head and the tail [3]. The relatively compact head region of high surface brightness is located in the northeast of the comet-shaped structure, while the diffuse tail region of low surface brightness extends to the southwest. From a bigger picture, the tail region is believed to break into a large low-density HI bubble, which may be created by the stellar wind and/or previous supernova explosions [4]. The most prominent structure of the head region is the pulsar wind nebula (PWN) Boomerang in the north, which is powered by the young and powerful pulsar PSR J2229+6114 with a characteristic age of 10 kyr and a high spin-down luminosity of 2.2×10^{37} erg s^{-1} [5]. A distance of 3 kpc of the system is estimated based on the X-ray absorption [6], but the shell-like structure of

HI wrapping around the SNR head, which is suggested to be interacting with the PWN–SNR complex, implies a physical distance of 800 pc of the system based on the velocity of the HI emission [4]. On the other hand, the molecular clouds found in the complex seem to have a different spatial distribution, with the location coincident with the tail region in our line of sight based on CO observations [4]. However, it is still uncertain whether the molecular clouds are directly disturbed by the SNR shocks [7], but they are expected to be nearby and thus can still be illuminated by the protons that escaped from the SNR [8,9].

Because of the special morphology, the PWN–SNR complex has drawn attention, and multi-wavelength data have been obtained. Radio observations have been pioneered, including one especially for the Boomerang Nebula [10]. The gamma-ray observations cover a large range from GeV to TeV, including detections by Fermi-LAT in the range of 0.1–500 GeV [11,12], by the Milagro collaboration at 20 TeV [13] as well as 35 TeV [14], and by the VERITAS collaboration in the range of 0.9–16 TeV [15] with the source named as VER J2227+608. Recently, HAWC [16] identified the target as HAWC J2227+610 and reported observations of gamma-ray emission up to 100 TeV. The Tibet ASγ [17] experiment also detected photons up to 100 TeV with measured emission centroid deviating from the pulsar's location at a confidence level of 3.1σ. Soon, LHAASO [1] lifted the maximum photon energy to 500 TeV.

The UHE ($E_\gamma \gtrsim 100$ TeV) gamma-rays are produced via inverse Compton (IC) scattering by electrons/positrons (hereafter, we do not distinguish positrons from electrons for simplicity) or via π^0 decay following the proton–proton collision. Several simulations have explored the leptonic or hadronic origin of the UHE emission [9,18–21]. Because of the spacial coincidence between the extended gamma-ray emission and the molecular clouds in the tail region, the hadronic origin of the TeV photons is favored (e.g., [8,17]). However, as an extended source, LHAASO J2226+6057 also partially covers the head region. This is also supported by the observations of VERITAS, HAWC and a recent preliminary analysis of MAGIC [22] at relatively lower energies. Therefore, we cannot totally exclude the possibility that the UHE photons, or at least part of them, originate from the PWN.

On the other hand, the nonthermal X-ray radiation traces UHE electrons and hence is useful for determining whether the origin of the UHE gamma-ray emission is leptonic or hadronic. Early study has only focused on PSR J2229+6114 and its vicinity [6], but recently, data from Chandra, XMM-Newton and Suzaku have been used to study the whole structure. X-ray spectra from different parts of the region follow power-law distributions [8], suggesting a nonthermal synchrotron origin of the X-ray emission. Interpreting the X-ray emission as thermal would invoke an unreasonably low metal abundance [23]. For reference, we summarize the X-ray observation, the UHE gamma-ray observtaion and the CO observation in Figure 1.

Ge et al. [8] (hereafter Ge2021) obtained radial profiles of X-ray surface brightness and photon index as a function of the distance from PSR J2229+6114, with a joint analysis of data from both Chandra and XMM-Newton. Figure 3A in Ge2021 shows the two radial profiles. Considering the trend of the profiles, they can be divided into three parts. The boundary between the first and second parts is about 100″ from the pulsar, which corresponds to the radius of the Boomerang Nebula, while the boundary between the second and third parts is about 840″ from the pulsar. In the first part, the surface brightness, or intensity, drops rapidly, while the photon index rises rapidly. This part is thought to be dominated by electrons confined in PWN. In the second part, the intensity continues to decline, but it is shallower than that of the first part, and the corresponding index also gently increases. Electrons escaping from the PWN are believed to contribute most in this area, corresponding to the head region. In the third part, the intensity and the photon index no longer change significantly. Due to the rapid cooling of the X-ray emitting electrons, X-ray emission from this part is most likely to be generated by electrons accelerated at the SNR shock. These two profiles show how the X-ray radiation varies spatially with the distance from the pulsar, and their characteristics suggest two different origins of the electrons, namely the PWN and the SNR.

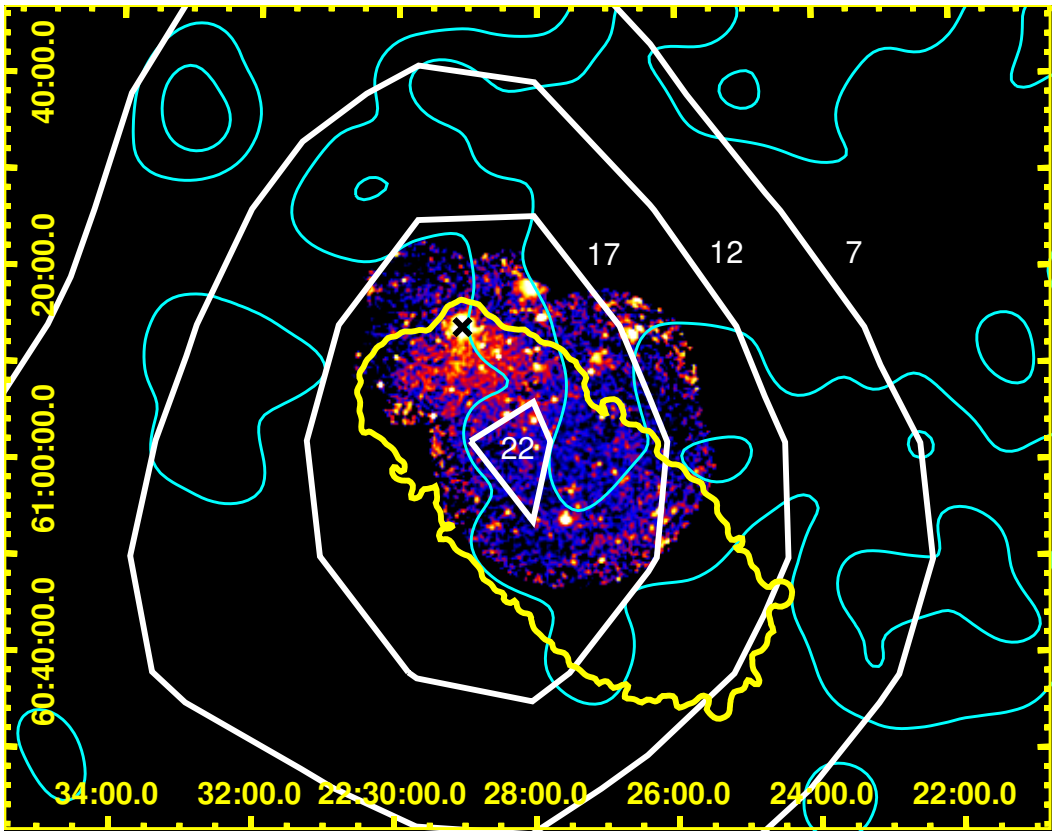


Figure 1. Observation results from different energy bands in equatorial coordinate system. The central-colored part is the combination of the X-ray observation from Chandra and XMM-Newton [8]. The pulsar position is marked with a black cross. The yellow curve outlines the 1.4 GHz radio continuum of the SNR [3]. The cyan contours show the CO emission of the molecular cloud [4]. The white contours show the LHAASO observation with numbers representing $\sqrt{\mathrm{TS}}$ values [1].

To further test this hypothesis, a numerical calculation is needed beyond the phenomenological analysis. In this paper, we model the X-ray profiles around the Boomerang Nebula obtained by Ge2021 with diffusing relativistic electrons injected in the PWN. The aim of the simulation is to explore the potential of the Boomerang Nebula as a PeVatron candidate.

The rest of this paper is organized as follows. The model is introduced in detail in Section 2. Section 3 presents the fitting result and the spectral energy distribution (SED). We discuss the simulation result and the possible contribution of UHE emission from the Boomerang Nebula in Section 4, and we finally draw a conclusion in Section 5.

2. Method

2.1. Two Electron Components

Since electrons have two different origins according to Ge2021, we consider two components in our simulations. For the SNR-accelerated electrons, we adopt the fitting results of the tail region from Ge2021. The electron distribution is described by a broken power-law with a super-exponential cutoff

$$\frac{\mathrm{d}N_e}{\mathrm{d}E_e} = N_{0,e}\left(\frac{E_e}{1\,\mathrm{TeV}}\right)^{-\alpha_e}\left[1+\left(\frac{E_e}{E_{e,\mathrm{b}}}\right)^{\sigma}\right]^{-\frac{\Delta\alpha_e}{\sigma}} e^{-\left(\frac{E_e}{E_{e,\mathrm{max}}}\right)^2}, \quad (1)$$

where α_e is the spectral index before the break, $\Delta\alpha_e$ is the index change when the energy exceeds the spectral break energy $E_{e,\mathrm{b}}$, σ is the smoothness of the spectral break, and $E_{e,\mathrm{max}}$ is the cutoff energy. $N_{0,e}$ is a normalization factor, which is determined by

$$\int E_e \frac{\mathrm{d}N_e}{\mathrm{d}E_e}\,\mathrm{d}E_e = W_e, \tag{2}$$

where the total energy W_e is obtained by fitting the data, and the limit of integration is from 5 MeV to 5 PeV. They use a $B = 20\,\mu\mathrm{G}$ magnetic field and fix σ to 5, and other parameters are obtained as $\alpha_e = 2.3$, $\Delta\alpha_e = 1.4$, $E_{e,\mathrm{b}} = 5\,\mathrm{MeV}$, $E_{e,\mathrm{max}} = 200\,\mathrm{TeV}$, and $W_e = 3 \times 10^{46}\,\mathrm{erg}$.

For PWN-originated electrons, we consider the temporal evolution of electrons injected from the pulsar's birth (i.e., $t = 0$) to the present time (i.e., $t = t_{age}$), following its spin-down history. Assuming the braking index $n = 3$, the dissipated rate of pulsar rotational energy, or spin-down luminosity, can be described by

$$L_t(t) = L_0\left(1 + \frac{t}{\tau_0}\right)^{-2}, \tag{3}$$

where

$$\tau_0 \equiv \frac{P_0}{2\dot{P}_0} = \tau_c - t_{age} \tag{4}$$

is the initial spin-down timescale of the pulsar. The age of the pulsar is given by

$$t_{age} = \frac{P}{2\dot{P}}\left[1 - \left(\frac{P_0}{P}\right)^2\right], \tag{5}$$

where P_0 is the initial rotation period of the pulsar. If $P_0 \ll P$, t_{age} will reduce to

$$\tau_c \equiv \frac{P}{2\dot{P}}, \tag{6}$$

which is called characteristic age and is an estimate of the age of the system. We assume that the injected electron distribution takes the form of an exponential cutoff power-law, and electrons are injected at a rate of

$$Q_{\mathrm{inj}}(E_e, t) \equiv \frac{\mathrm{d}N}{\mathrm{d}E_e \mathrm{d}t} = Q_0(t)\left(\frac{E_e}{1\,\mathrm{TeV}}\right)^{-p} e^{-\frac{E_e}{E_{\mathrm{cut}}}}, \tag{7}$$

where p is the spectral index of the injected electron spectrum, and E_{cut} is the cutoff energy. The normalization factor $Q_0(t)$ is determined by

$$\int E_e Q_{\mathrm{inj}}(E_e, t)\,\mathrm{d}E_e = \eta_e L_t(t), \tag{8}$$

where η_e is the efficiency at which the energy dissipated by pulsar rotation is converted to electron energy at the termination shock.

According to Kothes et al. [4], the elongated shape of the source is caused by the special environment. The radial profiles follow the direction of PWN–head–tail and thus can be assumed not to be affected by the possible reverse shock from the dense clouds in the northeast near the pulsar. Therefore, it is acceptable to consider the spherically symmetric propagation of electrons. In addition, we neglect the proper motion of the pulsar in the simulation for simplicity. The pulsar acts as a point source for the isotropic injection of electrons and the center of the sphere.

The general solution of the diffusion equation is incompatible with the theory of relativity at $r < 3D/c$, which leads to the phenomenon of superluminal propagation [24]. Because the rigorous solution in the relativistic case has not been obtained so far, it is necessary to modify the diffusion solution in a nonrelativistic case. One method is to

introduce ballistic propagation at a small radius. Following the approximation adapted by Recchia et al. [25], we use a critical time scale $t_c = 3D/c^2$ to distinguish ballistic propagation from diffusion propagation, where D is the diffusion coefficient and c is the speed of light. During a travelling time $t = \zeta t_c$, the ballistic and diffusive distances are $r_{ball} = ct = \zeta c t_c$ and $r_{diff} \sim \sqrt{Dt} = \sqrt{\zeta D t_c} \sim \sqrt{\zeta} c t_c$, respectively. For $\zeta < 1$, i.e., $t \lesssim t_c$, we will obtain $r_{ball} < r_{diff}$, suggesting the propagation speed in the diffusive regime exceeds the speed of light.

In our practical calculation, we adopt the generalized Jüttner function from Aloisio et al. [24] to consider both propagation mechanisms and connect them smoothly, i.e.,

$$P_J(E_e, r, t) = \frac{H(ct - r)}{4\pi(ct)^3} \frac{1}{\left[1 - \left(\frac{r}{ct}\right)^2\right]^2} \frac{y(E_e, t)}{K_1[y(E_e, t)]} \exp\left[-\frac{y(E_e, t)}{\sqrt{1 - \left(\frac{r}{ct}\right)^2}}\right], \tag{9}$$

where

$$y(E_e, t) = \frac{c^2 t^2}{2\lambda(E_e, t)}, \tag{10}$$

$$\lambda(E_e, t) = \int_t^{t_{age}} D\left[E'_e(t')\right] \mathrm{d}t'. \tag{11}$$

$H(x)$ is the Heaviside function, $K_1(x)$ is the first-order modified Bessel function of the second kind, and $E'_e(t')$ describes the change of electron energy over time. The existence of $H(x)$ avoids $v = r/t > c$ in the Jüttner function. To speed up calculation, we use an approximation (see Appendix A).

As electrons propagate outward, they suffer energy loss due to synchrotron radiation and IC radiation. The cooling rate is given by [26]

$$\dot{E}_e = -\frac{4}{3}\sigma_T c \left(\frac{E_e}{m_e c^2}\right)^2 \left\{U_B + \sum_i U_{\mathrm{ph},i} \Big/ \left[1 + \left(\frac{2.82 k T_i E_e}{m_e^2 c^4}\right)^{0.6}\right]^{\frac{1.9}{0.6}}\right\}, \tag{12}$$

where σ_T is the Thomson cross-section, m_e is the mass of the electron, c is the speed of light, and k is the Boltzmann constant. $U_B = B^2/8\pi$ is the magnetic field energy density, and $U_{\mathrm{ph},i}$ and T_i are the radiation field energy density and the corresponding temperature of the ith component, respectively. In addition to the CMB black body spectrum, three types of gray body photon fields in the interstellar medium of the Milky Way are included in the calculation of the energy loss caused by IC scattering. The specific parameters are listed in Table 1.

Table 1. Parameters of photon fields.

Photon Field	U_{ph} (eV cm^{-3})	T (K)
CMB	0.26	2.73
FIR	0.4	30
NIR	0.2	500
OPT	0.4	5000

After considering the pulsar injection, electron propagation and energy loss, the electron distribution at t_{age} can be expressed as

$$N(E_e, r) = \int_0^{t_{age}} Q_{\mathrm{inj}}(E_g, t) P_J(E_e, r, t) \frac{\mathrm{d}E_g}{\mathrm{d}E_e} \mathrm{d}t, \tag{13}$$

where E_e is the electron energy at the moment, and E_g is the initial energy of the electron injected at time t. Their relation and $\mathrm{d}E_g/\mathrm{d}E_e$ from Equation (13) can be obtained via Equation (12).

2.2. MCMC Modeling

Following the description in Section 2.1, we have obtained the spatial and spectral distributions of electrons that are injected from PWN at the present time. We have four free parameters: the electron injection spectral index p, the magnetic field B, and D_0 and δ from the energy-dependent diffusion coefficient

$$D(E) = D_0 \left(\frac{E_e}{100\,\mathrm{TeV}} \right)^{\delta}. \tag{14}$$

Other parameters are listed in Table 2, where the Lorentz factor $\gamma_e = \frac{E_e}{m_e c^2}$. Although the initial rotation period P_0 is also a free parameter, it barely influences the result unless it is very close to the current period $P = 51.6\,\mathrm{ms}$. Therefore, we fix it at 40 ms in our modeling, yielding $t_{\mathrm{age}} \approx 4200$ years.

Table 2. Fixed parameters of the model.

Parameter (Unit)	Value
n	3
P (s) [6]	0.0516
P_0 (s) [6]	0.04
$\dot{P}$ ($\mathrm{s\,s^{-1}}$) [6]	7.827×10^{-14}
L_s ($\mathrm{erg\,s^{-1}}$) [6]	2.2×10^{37}
d (pc) [4]	800
$\gamma_{inj,min}$	2×10^3
γ_{cut}	2×10^9

After obtaining the electron distribution, we can calculate the X-ray emission at 1–7 keV, which is dominated by synchrotron radiation, employing an acceleration method [27]. The next step is to integrate the emission along the line of sight. It is worth noting that the distribution of relativistic electrons is no longer angular symmetric during the transition from a ballistic to diffuse regime due to the introduction of ballistic propagation. We adopt the distribution from Prosekin et al. [28] as $\frac{1}{2\pi} M(\mu) = \frac{1}{2\pi Z(x)} e^{-\frac{3(1-\cos\mu)}{x}}$, where $Z(x) = \frac{x}{3}\left(1 - e^{-\frac{6}{x}}\right)$, $x(E) = \frac{rc}{D(E)}$, $\cos\mu = -\frac{r^2+s^2-d^2}{2rs}$, and $r = \sqrt{s^2 + d^2 - 2sd\cos\theta}$. d is the distance from the pulsar listed in Table 2, s is the distance from the integral position to the observer, r is the radial distance of the integral position from the pulsar, θ is the angle between the pulsar direction and the line of sight, and μ is the angle between the radial direction and the line of sight. It is obvious that the distribution is energy-dependent. To fit the surface brightness profile, we need to further integrate the intensity I over the range of 1–7 keV. For the SNR-accelerated electrons described in Section 2.1, Equation (2) yields a uniform electron distribution in the range of 600 arcmin^2. Similarly, we can obtain their synchrotron emission and the total intensity at 1–7 keV.

When fitting the observed data of radial profiles, we need to consider two kinds of electrons according to the analysis in Section 2.1. Following the picture raised by Ge2021, the PWN and the SNR dominate the X-ray emission at the head region and the tail region, respectively. Thus, we introduce a truncated angular distance θ_c for the SNR contribution to highlight the difference between the dominant positions of the two kinds of electrons, with the intensity of the SNR multiplied by a factor $e^{-\theta_c/\theta}$. Finally, we have six free parameters in the model: p, B, D_0, δ, η_e and θ_c.

Apart from the statistic error, we include an additional systematic error of 10% of the measured value due to the calibration uncertainties of instruments [29] in the fitting. We use the Markov chain Monte Carlo method (MCMC) to find the best fitting parameters with a Python package *emcee* [30]. The range of the six free parameters in the modeling is listed in Table 3, and B, D_0, η_e, and θ_c take logarithmic values based on 10 in MCMC. We

have 12 Markov chains in parallel, each running 5000 steps, of which the first 100 steps are regarded as burn-in and not included in the final sample.

Table 3. First row: model parameters; second row: searching range of parameters in MCMC; third row: best-fit values and 1σ uncertainties. Among the six parameters, B, D_0, η_e and θ_c take the logarithm in MCMC.

Parameter	p	B (μG)	D_0 ($\mathbf{cm^2\,s^{-1}}$)	δ	η_e	θ_c (arcsec)
range	$[1,3]$	$[1,10^3]$	$[10^{25},10^{30}]$	$[0,1]$	$[10^{-6},1]$	$[10,10^3]$
value ($\pm1\sigma$)	$2.1^{+0.13}_{-0.18}$	142^{+22}_{-22}	$1.5^{+1.1}_{-0.68}\times10^{29}$	$0.56^{+0.30}_{-0.36}$	$3.8^{+5.2}_{-2.1}\times10^{-4}$	75^{+99}_{-50}

3. Result

3.1. Fitting Result of the Radial Profiles

We put the best-fit values from MCMC into the model and obtain the fitting radial profiles of X-ray surface brightness and photon index of the PWN-SNR complex at 1–7 keV. The y-axis of the upper panel in Figure 2 is intensity, and that of the lower one is photon index, resembling Figure 3A from Ge2021. The best-fit values with uncertainties of each parameter obtained by the MCMC modeling are listed in Table 3. The χ^2 of the fitting is about 41 with 52 degrees of freedom. In this case, the cumulative probability reaches 68.3% at the 1σ level of the Gaussian distribution when $\Delta\chi^2 \approx 56$. We fix five parameters, decrease or increase the value of the remaining one, and substitute it into the model so that χ^2 reaches approximately 97. After performing the above procedure on all parameters, we obtain the fitting curves corresponding to 12 groups of parameters. The boundary values enclosed by all curves are taken as the final error band.

The fitting curve in Figure 2 can well reproduce the profiles of both X-ray surface brightness and photon index. The relatively strong magnetic field $B = 142\,\mu$G is worthy of note, as the magnetic field energy density U_B reaches about $500\,\mathrm{eV/cm^3}$, which is much larger than the radiation field energy density listed in Table 1. The IC scattering of electrons is severely suppressed under such circumstances, and high-energy gamma-ray photons are thus difficult to be produced by PWN-accelerated electrons, which is consistent with the observation of the head region by Fermi-LAT [18]. Note that in an earlier study [10], an even stronger magnetic field of $B = 2.6$ mG for the PWN was proposed through ascribing the spectral break at 4.3 GHz to the synchrotron cooling. With a smaller magnetic field, we ascribe the radio break to the minimum energy in the injected electron spectrum.

3.2. Spectral Energy Distribution

LHAASO detected significant signals of UHE photons well above 100 TeV in this PWN-SNR complex, and the angular extension of the UHE emission covers part of the head region. Therefore, we cannot completely exclude the possibility of part of the UHE emission originating from Boomerang. The large magnetic field obtained from the fitting of X-ray profiles implies a significant suppression of the inverse Compton radiation of electrons. On the other hand, the LHAASO collaboration [26] perceived a possible hardening of energy spectrum near 1 PeV in the Crab Nebula. The standard one-component model could not explain this feature, and an alternative two-component scenario was proposed, where the additional component could be either electron or proton. Enlightened by their work, we envisage that a second spectral component may also exist in Boomerang and could possibly account for part of the UHE emission detected by LHAASO in this region. It may be worth mentioning that although the leptonic origin of gamma-rays is the standard picture for PWN, the hadronic origin has been suggested and studied by many previous studies (e.g., [31–36]).

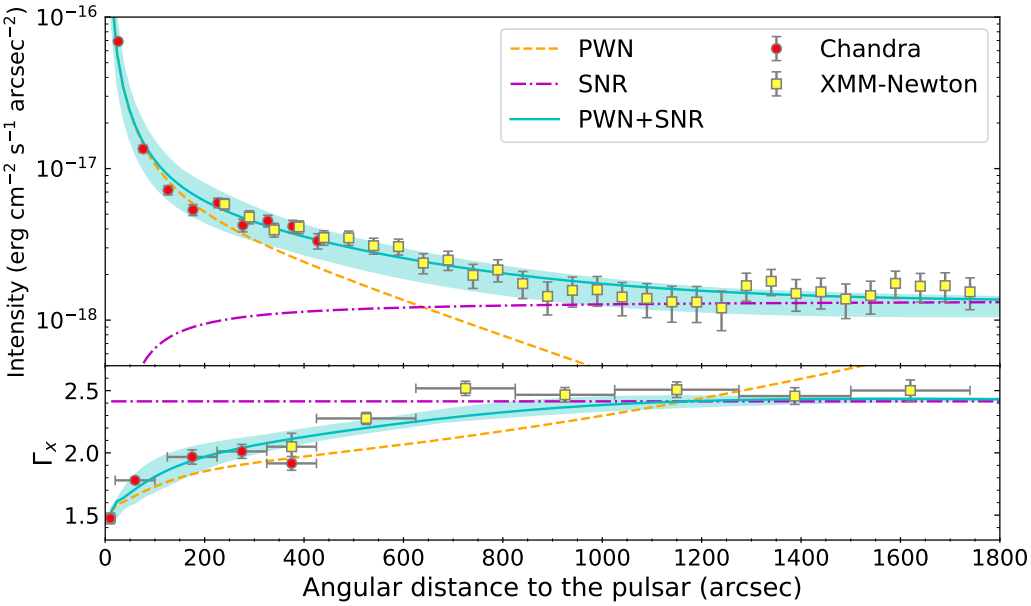


Figure 2. The fitting result of the radial profiles of X-ray surface brightness and photon index. The orange dashed line represents the PWN electron component, the purple dash–dotted line represents the SNR electron component, and the cyan solid line with a 1σ error band is the sum of the two. Red and yellow data points are from Chandra and XMM-Newton, respectively, taken from Ge2021. Only statistic errors are shown.

To check the possibility of this scenario, we assume two particle components in the PWN. The first electron component, which accounts for the X-ray emission, follows a power-law distribution with exponential cutoff, i.e.,

$$\frac{\mathrm{d}N_e}{\mathrm{d}E_e} = N_{0,e}\left(\frac{E_e}{1\,\mathrm{TeV}}\right)^{-\alpha_e} e^{-\frac{E_e}{E_{e,\mathrm{cut}}}}. \tag{15}$$

Note that this component is supposed to be the same as the one modeled in Section 3.1 for the X-ray emission, after spatial integration. Similar to LHAASO's treatment, we also consider an additional electron component (i.e., the two-component leptonic scenario) or a proton component (i.e., the lepto-hadronic scenario) as the second particle component. The emission of the second component is set to contribute half of the measured flux at 500 TeV by LHAASO.

In the former scenario, the second electron component is assumed to follow the Maxwellian distribution [37], i.e.,

$$\frac{\mathrm{d}N_m}{\mathrm{d}E_m} = N_{0,m}\left(\frac{E_m}{1\,\mathrm{TeV}}\right)^{2} e^{-\frac{E_m}{E_{m,\mathrm{cut}}}}. \tag{16}$$

The generated energy spectrum is shown in the left panel of Figure 3, using the previously obtained best-fit magnetic field of $B = 142\,\mu$G and photon fields listed in Table 1. Other fitting parameters are listed in Table 4. The rather weak IC radiation of the Maxwellian-type electrons appears near 100 TeV, peaks around 1 PeV, and drops rapidly. Remarkably, the synchrotron radiation of the Maxwellian type forms a significant bump in the MeV band, peaking at about 100 MeV. The huge protuberance has a much higher flux and harder spectrum compared to the measurement from both Chandra and NuSTAR, making this scenario unlikely to be realistic. A possible way of avoiding the X-ray constraints in this case would be invoking an even narrower distribution than the Maxwellian distribution for the spectrum of the second electron component; however, the formation mechanism is unclear.

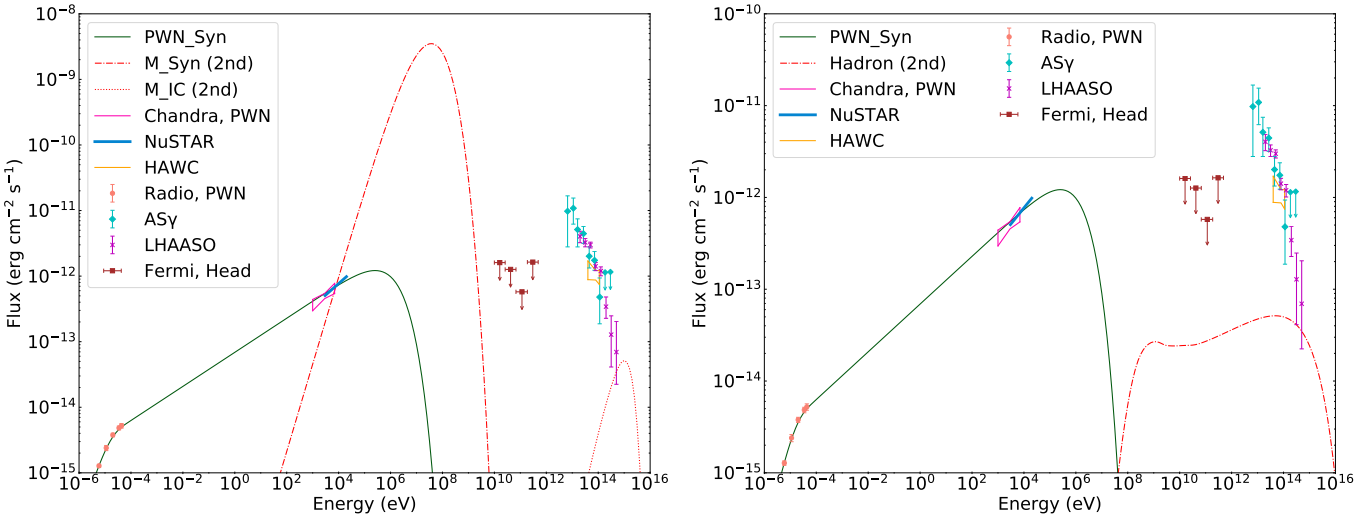


Figure 3. Left panel: The two-component leptonic scenario for the head region. The dark green solid line is the synchrotron radiation of the power-law type electrons, and the red dash–dotted and dotted lines are the synchrotron and IC radiation of the Maxwellian-type electrons, respectively. The salmon points on the left are the radio data from Kothes et al. [10], and the bright pink butterfly plot is from the observation of Chandra in Ge2021. The recent NuSTAR measurement at 3–20 keV is also shown in cerulean [38]. The brown upper limit of the GeV band comes from the Fermi-LAT observation of the head region [18], while the cyan and magenta TeV data points and orange butterfly plot on the right are from ASγ [17], LHAASO [1], and HAWC [16], respectively. The GeV–TeV observations are not involved in the fitting, since most of them are spatially coincident with the tail region, and they are shown for reference only. **Right panel**: The lepto-hadronic scenario. The dark green solid line represents the synchrotron radiation of electrons, and the red dash–dotted line represents gamma-ray radiation from π^0 decay.

Table 4. Fitting parameters of the two-component leptonic scenario and lepto-hadronic scenario, corresponding to Figure 3. The former comprises the PWN electron component (first row) plus the Maxwellian type (second row), and the latter comprises the PWN electron component (first row) plus proton component (third row).

1st e (Equation (15))	α_e 2.5	$E_{e,\mathrm{cut}}$ (eV) 4.0×10^{14}	$E_{e,\mathrm{min}}$ (eV) 1.0×10^{9}	W_e (erg) 1.3×10^{43}
2nd e (Equation (16))	$E_{m,\mathrm{cut}}$ (eV) 4.0×10^{14}	$E_{m,\mathrm{min}}$ (eV) 1.0×10^{12}	W_m (erg) 7.5×10^{42}	
p (Equation (17))	α_p 2.0	$E_{p,\mathrm{cut}}$ (eV) 1.0×10^{16}	W_p (erg) 1.3×10^{46}	n_{gas} (cm^{-3}) 10

As for the lepto-hadronic scenario, the additional proton component follows the same form as the electron given by

$$\frac{\mathrm{d}N_p}{\mathrm{d}E_p} = N_{0,p}\left(\frac{E_p}{1\,\mathrm{TeV}}\right)^{-\alpha_p} e^{-\frac{E_p}{E_{p,\mathrm{cut}}}}. \quad (17)$$

We follow the semi-analytical method developed by Kafexhiu et al. [39] to calculate the pionic gamma-ray spectra generated by the proton–proton collisions. A flat proton injection spectrum (i.e., $\alpha_p = 2$) is employed in the following calculation as an example, noting that the proton spectral index is not a well-determined parameter here. If the TeV gamma-ray emission from the head region as revealed by the preliminary MAGIC data [22] also originates from this proton component, a steeper injection spectrum would be needed. The magnetic field and photon fields are the same as the previous case, and the remaining parameters are listed in Table 4, where n_{gas} is the gas density. As we can see in the right

panel of Figure 3, gamma-ray emission rises to a certain flux in the GeV band, peaks at several hundred TeV and remains high at 1 PeV before dropping. The proton population still contributes a small amount of energy flux up to 10 PeV compared to the rapid drop in the two-electron case. Assuming the moment of inertia of the pulsar to be 10^{45} g cm^2 and using the initial and present pulsar period in Table 2, the total spin-down energy dissipated since its birth is 4.9×10^{48} erg, according to $E_{rot} = \frac{1}{2} I (2\pi/P)^2$. It is greater than the sum of the energies of the electron and proton, so the scenario does not violate the conservation of energy. Therefore, if the future observations reveal that part of the UHE gamma-ray emission arises from the Boomerang Nebula, our analysis will indicate that Boomerang Nebula, probably as well as other energetic PWNe, is a proton PeVatron.

4. Discussion

Although the fitting result of the radial profiles is fairly good, there are some limited aspects of the model. First, we assume a homogeneous magnetic field and diffusion coefficient in the model, which is a simplified assumption and may not be the reality. If variations of the magnetic field or the diffusion coefficient are taken into account, a more complete conclusion will be reached. Second, we only consider diffusive transport of particles in the PWN, which has been suggested for many other PWNe [40–44]. However, other transport mechanisms such as advection may also have an important effect on the electron distribution (e.g., [45–47]). Last, we cannot ignore the complexity of the surrounding environment of the PWN. The isotropic propagation may be a simplification, as the shape of Boomerang is irregular, and the reverse shock generated by the dense clouds in the northeast may also affect the acceleration and propagation of particles.

Hence, we try attesting to the result from another perspective. If the electrons from the PWN can substantially contribute to the UHE gamma-ray emission, a weaker magnetic field will be required. Thus, we estimate the lower limit of the magnetic field, with an ideal (and probably unrealistic) assumption that introducing the aforementioned effects in the particle transport can somehow reproduce the profiles of X-ray emission with a relatively weak magnetic field. In this optimistic limit, a basic requirement for the magnetic field is to make the electrons that emit X-ray photons cool down so as to explain the rapid increase of the photon index in the PWN region within 100″. Therefore, we have

$$\tau_c \geq t_{\rm syn} \sim \frac{E_e}{P_{\rm syn}} = \frac{\gamma m c^2}{\frac{4}{3}\sigma_T c \gamma^2 U_B}. \quad (18)$$

Here, we employ τ_c instead of $t_{\rm age}$ as a conservative requirement of the cooling timescale in the system. The Lorentz factor can be replaced according to $\nu_c = 3\gamma^2 eB/4\pi mc$, where ν_c is the critical frequency of the synchrotron emission. Therefore, to make keV-emitting electrons cool within τ_c, a lower limit of magnetic field $B_{\rm c,LL} = 4.7\,\mu$G will be obtained. On the other hand, the Hillas condition [48] requires $B \gtrsim E_e/eR$, where R corresponds to the termination shock radius of about 0.1 pc with a reference to the Crab [26,49]. The emitted gamma-ray photon energy via the IC mechanism can be estimated via $E_{IC} \sim E_e\,\Gamma/(1+\Gamma)$, where $\Gamma = \gamma\epsilon/mc^2$. ϵ is the average photon energy of the radiation field, and for a black body or gray body radiation, it can be expressed as $\epsilon = 2.82kT$. Here, we use the CMB field as the radiation field. To scatter CMB photons up to $E_{\rm IC} = 500$ TeV, the corresponding electron energy needs to be $E_e \approx 760$ TeV. If we substitute this energy into the Hillas condition, we will obtain a lower limit of magnetic field $B_{\rm H,LL} = 8.2\,\mu{\rm G} > B_{\rm c,LL}$. Similar to the two-component leptonic scenario described in Section 3.2, we fit the SED again using $B_{\rm H,LL}$ and other parameters listed in Table 5, as shown in Figure 4.

We see that with the weaker magnetic field, the IC flux from the first electron component can contribute a small amount of energy flux at several hundred TeV, but it is still far less than the measured values. If we still attribute half of the measured flux at 500 TeV to the second electron component, a prominent synchrotron bump peaking at the MeV regime will still be expected, although it is not as towering as the one in the left panel of Figure 3. It is not in contrast with the current observation, but the next-generation MeV

gamma-ray instruments such as e-ASTROGAM [50] and AMEGO [51] will be helpful to discern this scenario.

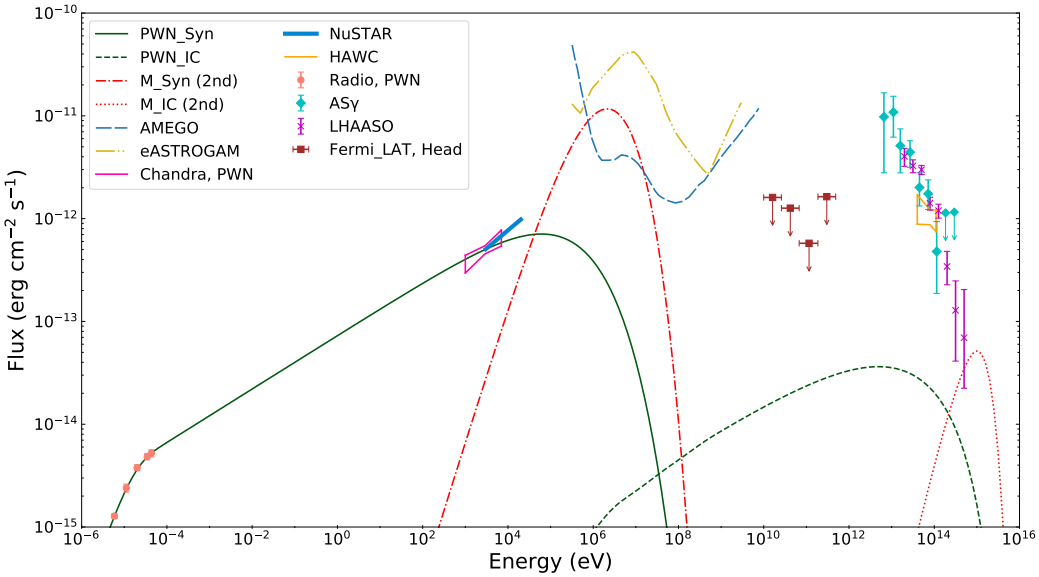


Figure 4. The two-component leptonic scenario for the head region. The dark green solid and dashed lines are the synchrotron and IC radiation of the power-law type electrons, respectively, and the red dash–dotted and dotted lines are the synchrotron and IC radiation of the Maxwellian-type electrons, respectively. The gold dash–dot–dotted curve and the blue dashed curve show the 1 Ms sensitivity of the next-generation MeV gamma-ray detectors e-ASTROGAM [50] and AMEGO [51], respectively. Observation data are the same as the ones in Figure 3.

Table 5. Fitting parameters of the two-component leptonic scenario with a relatively weaker magnetic field, corresponding to Figure 4.

α_1	$E_{1,\mathrm{cut}}$ (eV)	$E_{1,\mathrm{min}}$ (eV)	W_1 (erg)	$E_{2,\mathrm{cut}}$ (eV)	$E_{2,\mathrm{min}}$ (eV)	W_2 (erg)
2.5	7.6×10^{14}	4.4×10^{9}	9.6×10^{44}	4.0×10^{14}	1.0×10^{12}	7.5×10^{42}

5. Conclusions

Based on the radial profiles of X-ray surface brightness and photon index of the PWN-SNR complex at 1–7 keV obtained by Ge2021, we study the X-ray emission of the PWN Boomerang by numerical simulation. In the diffusion framework, we introduce ballistic propagation and use the Jüttner function to describe electron transport. Considering the pulsar injection history, the electron transport and the radiation energy loss, we simulate the evolution from the birth of PSR J2229+6114 to the current time of t_{age} to obtain the distribution of PWN accelerated electrons at present. Including both the PWN electrons and the SNR electrons described in Ge2021, we use the MCMC method to fit the radial profiles. The fitting curve obtained by taking the best-fit values as the model parameters can reproduce the two profiles at the same time. Under the condition of the derived strong PWN magnetic field $B = 142\,\mu$G, the IC scattering of electrons is severely suppressed, and it is difficult to produce gamma-ray radiation, which is consistent with Fermi-LAT observation of the head region of the SNR. However, due to the lack of UHE gamma-ray observations of Boomerang and its vicinity, its possible PeVatron nature cannot be ruled out.

Referring to the interpretation by the LHAASO collaboration of the possible hardening of the energy spectrum of the Crab Nebula at 1 PeV, we attempt to simulate the spectra of Boomerang producing UHE gamma-ray radiation by adding a second component of particles, either electrons or protons. For the two-component leptonic scenario, the rather weak IC radiation of the Maxwellian-type electron reaches its peak at 1 PeV and then decreases rapidly. In addition, there is a prominent bump in the MeV band, making this

scenario unlikely as it contradicts the measurement from Chandra and NuSTAR. In the case of adding a proton population, it can account for UHE gamma-ray emission, at least a considerable fraction, with reasonable parameters. The energy spectrum of the proton component extends beyond 1 PeV. In other words, if a fraction of the UHE gamma-ray photons of LHAASO J2226+6057 truly comes from Boomerang Nebula, it would indicate that the PWN is a hadronic PeVatron. This scenario would require detectors such as LHAASO to confirm in the future.

Furthermore, we discuss the possible scenario with a relatively weaker, albeit unjustified, magnetic field of the PWN. Employing the lower limit of $B = 8.2\,\mu$G derived from the Hillas condition for the acceleration of electrons emitting 500 TeV photons, a second electron component of Maxwellian-type spectral distribution can interpret the UHE emission via the IC process without violating the current X-ray observations, but it still results in a bump in the spectrum at the MeV band. Next-generation MeV gamma-ray instruments can be helpful to discern this case.

Author Contributions: Investigation, Q.-Z.W. and J.-S.P.; Methodology, X.-H.L.; Project administration, R.-Y.L.; Software, C.-M.L.; Supervision, R.-Y.L.; Validation, Q.-Z.W. and J.-S.P.; Visualization, X.-H.L.; Writing—original draft, X.-H.L.; Writing—review & editing, C.-M.L. and R.-Y.L. All authors have read and agreed to the published version of the manuscript.

Funding: This work is supported by NSFC under grant No. U2031105.

Acknowledgments: We thank Chong Ge for helpful discussion on systematic errors of X-ray measurements.

Conflicts of Interest: The authors declare no conflict of interest.

Appendix A. The Jüttner Function

The ultrarelativistic particles travel with $v \approx c$ in the ballistic regime. As time goes by, they experience multiple deflections caused by the turbulent magnetic field, resulting in the transition to diffusion and the isotropization of the particle directions. We employ the generalized Jüttner function to describe this transition, and its original form in Aloisio et al. [24] is already given by Equations (9) and (10). The approximation utilized for speeding up is written as

$$Z(y)e^{y} \sim \frac{y}{K_1(y)}, \tag{A1}$$

where

$$Z(y) = \frac{y^2}{\left[1 + \left(\frac{\pi}{2}y\right)^{\frac{0.5}{0.53}}\right]^{0.53}}. \tag{A2}$$

To verify the accuracy of the approximation, we plot the functions from both sides of Equation (A1) in Figure A1. It is obvious that the values of the two functions are very close over a range of five orders of magnitude. To further demonstrate, the ratio of the two values always fluctuates around unity, with the maximum relative error being only 0.23%. Hence, the approximation is accurate enough to be used for speeding up calculation. Eventually, the Jüttner function we used is written as

$$P_J(E_e, r, t) = \frac{H(ct-r)}{4\pi(ct)^3} \frac{1}{\left[1 - \left(\frac{r}{ct}\right)^2\right]^2} Z[y(E_e,t)] \exp\left[y(E_e,t) - \frac{y(E_e,t)}{\sqrt{1-\left(\frac{r}{ct}\right)^2}}\right]. \tag{A3}$$

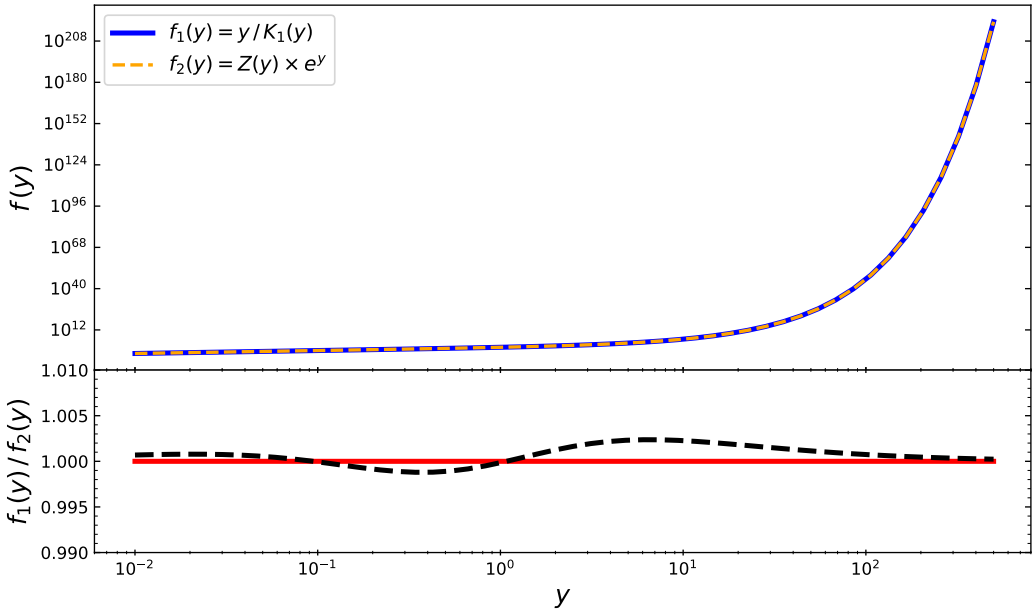


Figure A1. Comparison between functions from both sides of Equation (A1). The upper panel shows the two functions over five orders of magnitude, with the orange dashed line denoting the left side of Equation (A1) and the blue solid line denoting the right side of Equation (A1) from Jüttner distribution. The lower panel shows the ratio of the value of the original function to the approximate value of the substitute in the black dashed line, with the red solid line being unity for reference.

References

1. Cao, Z.; Aharonian, F.; An, Q.; Bai, L.; Bai, Y.; Bao, Y.; Bastieri, D.; Bi, X.; Bi, Y.; Cai, H.; et al. Ultrahigh-energy photons up to 1.4 petaelectronvolts from 12 γ-ray Galactic sources. *Nature* **2021**, *594*, 33–36. [CrossRef] [PubMed]
2. Joncas, G.; Higgs, L. The DRAO galactic-plane survey. II-Field at L = 105 deg. *Astron. Astrophys. Suppl. Ser.* **1990**, *82*, 113–144.
3. Pineault, S.; Joncas, G. G106. 3+ 2.7: A supernova remnant in a late stage of evolution. *Astron. J.* **2000**, *120*, 3218. [CrossRef]
4. Kothes, R.; Uyaniker, B.; Pineault, S. The supernova remnant G106. 3+ 2.7 and its pulsar-wind nebula: Relics of triggered star formation in a complex environment. *Astrophys. J.* **2001**, *560*, 236. [CrossRef]
5. Halpern, J.P.; Gotthelf, E.; Leighly, K.; Helfand, D. A possible X-ray and radio counterpart of the high-energy gamma-ray source 3EG J2227+ 6122. *Astrophys. J.* **2001**, *547*, 323. [CrossRef]
6. Halpern, J.; Camilo, F.; Gotthelf, E.; Helfand, D.; Kramer, M.; Lyne, A.; Leighly, K.; Eracleous, M. PSR J2229+ 6114: Discovery of an energetic young pulsar in the error box of the EGRET source 3EG J2227+ 6122. *Astrophys. J.* **2001**, *552*, L125. [CrossRef]
7. Liu, Q.C.; Zhou, P.; Chen, Y. IRAM 30 m CO-line Observation toward the PeVatron Candidate G106. 3+ 2.7: Direct Interaction between the Shock and the Molecular Cloud Remains Uncertain. *Astrophys. J.* **2022**, *926*, 124. [CrossRef]
8. Ge, C.; Liu, R.Y.; Niu, S.; Chen, Y.; Wang, X.Y. Revealing a peculiar supernova remnant G106. 3+ 2.7 as a petaelectronvolt proton accelerator with X-ray observations. *Innovation* **2021**, *2*, 100118.
9. Bao, Y.; Chen, Y. On the Hard Gamma-Ray Spectrum of the Potential PeVatron Supernova Remnant G106. 3+ 2.7. *Astrophys. J.* **2021**, *919*, 32. [CrossRef]
10. Kothes, R.; Reich, W.; Uyanıker, B. The Boomerang PWN G106. 6+ 2.9 and the magnetic field structure in pulsar wind nebulae. *Astrophys. J.* **2006**, *638*, 225. [CrossRef]
11. Xin, Y.; Zeng, H.; Liu, S.; Fan, Y.; Wei, D. VER J2227+ 608: A hadronic pevatron pulsar wind nebula? *Astrophys. J.* **2019**, *885*, 162. [CrossRef]
12. Fang, K.; Kerr, M.; Blandford, R.; Fleischhack, H.; Charles, E. Evidence for PeV Proton Acceleration from Fermi-LAT Observations of SNR G 106.3+ 2.7. *Phys. Rev. Lett.* **2022**, *129*, 071101. [CrossRef] [PubMed]
13. Abdo, A.A.; Allen, B.; Berley, D.; Casanova, S.; Chen, C.; Coyne, D.; Dingus, B.; Ellsworth, R.; Fleysher, L.; Fleysher, R.; et al. TeV gamma-ray sources from a survey of the galactic plane with Milagro. *Astrophys. J.* **2007**, *664*, L91. [CrossRef]
14. Abdo, A.; Allen, B.; Aune, T.; Berley, D.; Chen, C.; Christopher, G.; DeYoung, T.; Dingus, B.; Ellsworth, R.; Gonzalez, M.; et al. Milagro observations of multi-TeV emission from Galactic sources in the Fermi bright source list. *Astrophys. J.* **2009**, *700*, L127. [CrossRef]
15. Acciari, V.; Aliu, E.; Arlen, T.; Aune, T.; Bautista, M.; Beilicke, M.; Benbow, W.; Boltuch, D.; Bradbury, S.; Buckley, J.; et al. Detection of extended VHE gamma ray emission from G106. 3+ 2.7 with veritas. *Astrophys. J.* **2009**, *703*, L6. [CrossRef]

16. Albert, A.; Alfaro, R.; Alvarez, C.; Camacho, J.A.; Arteaga-Velázquez, J.; Arunbabu, K.; Rojas, D.A.; Solares, H.A.; Baghmanyan, V.; Belmont-Moreno, E.; et al. HAWC J2227+ 610 and its association with G106. 3+ 2.7, a new potential galactic PeVatron. *Astrophys. J. Lett.* **2020**, *896*, L29. [CrossRef]
17. Amenomori, M.; Bao, Y.; Bi, X.; Chen, D.; Chen, T.; Chen, W.; Chen, X.; Chen, Y.; Cirennima, C.; Danzengluobu, D.; et al. Potential PeVatron supernova remnant G106. 3+ 2.7 seen in the highest-energy gamma rays. *Nat. Astron.* **2021**, *5*, 460–464.
18. Liu, S.; Zeng, H.; Xin, Y.; Zhu, H. Hadronic versus leptonic models for γ-ray emission from VER J2227+ 608. *Astrophys. J. Lett.* **2020**, *897*, L34. [CrossRef]
19. Yu, H.; Wu, K.; Wen, L.; Fang, J. A leptonic model for the γ-rays coincident with the tail region of the supernova remnant G106. 3+ 2.7. *New Astron.* **2022**, *90*, 101669. [CrossRef]
20. Yang, C.; Zeng, H.; Bao, B.; Zhang, L. Possible hadronic origin of TeV photon emission from SNR G106. 3+ 2.7. *Astron. Astrophys.* **2022**, *658*, A60. [CrossRef]
21. Breuhaus, M.; Reville, B.; Hinton, J. Pulsar wind nebula origin of the LHAASO-detected ultra-high energy γ-ray sources. *Astron. Astrophys.* **2022**, *660*, A8. [CrossRef]
22. The MAGIC Collaboration; Acciari, V.A.; Ansoldi, S.; Antonelli, L.A.; Arbet Engels, A.; Artero, M.; Asano, K.; Baack, D.; Babic, A.; Baquero, A.; et al. Resolving the origin of very-high-energy gamma-ray emission from the PeVatron candidate SNR G106.3+2.7 using MAGIC telescopes. In Proceedings of the 37th International Cosmic Ray Conference, Berlin, Germany, 12–23 July 2021; p. 796.
23. Fujita, Y.; Bamba, A.; Nobukawa, K.K.; Matsumoto, H. X-ray Emission from the PeVatron-candidate Supernova Remnant G106. 3+ 2.7. *Astrophys. J.* **2021**, *912*, 133. [CrossRef]
24. Aloisio, R.; Berezinsky, V.; Gazizov, A. The problem of superluminal diffusion of relativistic particles and its phenomenological solution. *Astrophys. J.* **2009**, *693*, 1275. [CrossRef]
25. Recchia, S.; Di Mauro, M.; Aharonian, F.A.; Orusa, L.; Donato, F.; Gabici, S.; Manconi, S. Do the Geminga, Monogem and PSR J0622+ 3749 γ-ray halos imply slow diffusion around pulsars? *Phys. Rev. D* **2021**, *104*, 123017. [CrossRef]
26. Cao, Z.; Aharonian, F.; An, Q.; Axikegu; Bai, L.; Bai, Y.; Bao, Y.; Bastieri, D.; Bi, X.J.; Bi, Y.J.; et al. Peta–electron volt gamma-ray emission from the Crab Nebula. *Science* **2021**, *373*, 425–430. [PubMed]
27. Fouka, M.; Ouichaoui, S. Analytical fits to the synchrotron functions. *Res. Astron. Astrophys.* **2013**, *13*, 680. [CrossRef]
28. Prosekin, A.Y.; Kelner, S.R.; Aharonian, F.A. Transition of propagation of relativistic particles from the ballistic to the diffusion regime. *Phys. Rev. D* **2015**, *92*, 083003. [CrossRef]
29. Schellenberger, G.; Reiprich, T.H.; Lovisari, L.; Nevalainen, J.; David, L. XMM-Newton and Chandra cross-calibration using HIFLUGCS galaxy clusters. Systematic temperature differences and cosmological impact. *Astron. Astrophys.* **2015**, *575*, A30, [CrossRef]
30. Foreman-Mackey, D.; Hogg, D.W.; Lang, D.; Goodman, J. emcee: The MCMC hammer. *Publ. Astron. Soc. Pac.* **2013**, *125*, 306. [CrossRef]
31. Atoyan, A.M.; Aharonian, F.A. On the mechanisms of gamma radiation in the Crab Nebula. *Mon. Not. R. Astron. Soc. Lett.* **1996**, *278*, 525–541. [CrossRef]
32. Amato, E.; Guetta, D.; Blasi, P. Signatures of high energy protons in pulsar winds. *Astron. Astrophys.* **2003**, *402*, 827–836. [CrossRef]
33. Zhang, L.; Yang, X.C. TeV Gamma-Ray Emission from Vela X: Leptonic or Hadronic? *Astrophys. J.* **2009**, *699*, L153–L156. [CrossRef]
34. Li, H.; Chen, Y.; Zhang, L. Lepto-hadronic origin of γ-rays from the G54.1+0.3 pulsar wind nebula. *Mon. Not. R. Astron. Soc. Lett.* **2010**, *408*, L80–L84. [CrossRef]
35. Di Palma, I.; Guetta, D.; Amato, E. Revised Predictions of Neutrino Fluxes from Pulsar Wind Nebulae. *Astrophys. J.* **2017**, *836*, 159. [CrossRef]
36. Liu, R.Y.; Wang, X.Y. PeV Emission of the Crab Nebula: Constraints on the Proton Content in Pulsar Wind and Implications. *Astrophys. J.* **2021**, *922*, 221. [CrossRef]
37. Aharonian, F.A.; Atoyan, A.M. Nonthermal Radiation of the Crab Nebula. In Proceedings of the Neutron Stars and Pulsars: Thirty Years after the Discovery, Tokyo, Japan, 17–20 November 1997; Shibazaki, N., Ed.; Universal Academy Press: Tokyo, Japan, 1998; p. 439.
38. Mori, K.; An, H.; Burgess, D.; Capasso, M.; Dingus, B.; Gelfand, J.; Hailey, C.; Humensky, B.; Malone, K.; Mukherjee, R.; et al. NuSTAR broad-band X-ray observational campaign of energetic pulsar wind nebulae in synergy with VERITAS, HAWC and Fermi gamma-ray telescopes. In Proceedings of the 37th International Cosmic Ray Conference, Berlin, Germay, 12–23 July 2021; p. 963.
39. Kafexhiu, E.; Aharonian, F.; Taylor, A.M.; Vila, G.S. Parametrization of gamma-ray production cross sections for p p interactions in a broad proton energy range from the kinematic threshold to PeV energies. *Phys. Rev. D* **2014**, *90*, 123014. [CrossRef]
40. Tang, X.; Chevalier, R.A. Particle Transport in Young Pulsar Wind Nebulae. *Astrophys. J.* **2012**, *752*, 83. [CrossRef]
41. Porth, O.; Vorster, M.J.; Lyutikov, M.; Engelbrecht, N.E. Diffusion in pulsar wind nebulae: An investigation using magnetohydrodynamic and particle transport models. *Mon. Not. R. Astron. Soc. Lett.* **2016**, *460*, 4135–4149. [CrossRef]
42. Bao, Y.; Liu, S.; Chen, Y. On the Gamma-Ray Nebula of Vela Pulsar. I. Very Slow Diffusion of Energetic Electrons within the TeV Nebula. *Astrophys. J.* **2019**, *877*, 54. [CrossRef]

43. Liu, R.Y.; Yan, H. On the unusually large spatial extent of the TeV nebula HESS J1825-137: Implication from the energy-dependent morphology. *Mon. Not. R. Astron. Soc. Lett.* **2020**, *494*, 2618–2627. [CrossRef]
44. Hu, C.P.; Ishizaki, W.; Ng, C.Y.; Tanaka, S.J.; Mong, Y.L. A Comprehensive Study of the Spectral Variation and the Brightness Profile of Young Pulsar Wind Nebulae. *Astrophys. J.* **2022**, *927*, 87. [CrossRef]
45. Kennel, C.F.; Coroniti, F.V. Magnetohydrodynamic model of Crab nebula radiation. *Astrophys. J.* **1984**, *283*, 710–730. [CrossRef]
46. Van Etten, A.; Romani, R.W. Multi-zone Modeling of the Pulsar Wind Nebula HESS J1825-137. *Astrophys. J.* **2011**, *742*, 62. [CrossRef]
47. Ishizaki, W.; Asano, K.; Kawaguchi, K. Outflow and Emission Model of Pulsar Wind Nebulae with the Back Reaction of Particle Diffusion. *Astrophys. J.* **2018**, *867*, 141. [CrossRef]
48. Hillas, A.M. The Origin of Ultra-High-Energy Cosmic Rays. *Annu. Rev. Astron. Astrophys.* **1984**, *22*, 425–444. [CrossRef]
49. Gaensler, B.M.; Slane, P.O. The evolution and structure of pulsar wind nebulae. *Annu. Rev. Astron. Astrophys.* **2006**, *44*, 17–47. [CrossRef]
50. De Angelis, A.; Tatischeff, V.; Tavani, M.; Oberlack, U.; Grenier, I.; Hanlon, L.; Walter, R.; Argan, A.; von Ballmoos, P.; Bulgarelli, A.; et al. The e-ASTROGAM mission. Exploring the extreme Universe with gamma rays in the MeV–GeV range. *Exp. Astron.* **2017**, *44*, 25–82. [CrossRef]
51. Moiseev, A.; Amego Team. All-Sky Medium Energy Gamma-ray Observatory (AMEGO). In Proceedings of the 35th International Cosmic Ray Conference (ICRC2017), Busan, Korea, 12–20 July 2017; Volume 301, p. 798.